Multiphonon Transitions in a Quantum Electromechanical System

Multiphonon Transitions in a Quantum Electromechanical System

Alpo Välimaa,[1,†] Wayne Crump,[1,†] Mikael Kervinen,[1,2] and Mika A. Sillanpää[1,*]

[1] *Department of Applied Physics, Aalto University, P.O. Box 15100, AALTO FI-00076, Finland*

[2] *Department of Microtechnology and Nanoscience MC2, Chalmers University of Technology, Göteborg SE-412 96, Sweden*

(Received 13 August 2021; revised 5 January 2022; accepted 20 April 2022; published 1 June 2022)

Studies of micromechanical and acoustic modes in the quantum regime have shed light on quantum properties of massive objects. Integrating these systems into superconducting circuits shows great promise for applications as quantum memory elements, bosonic codes, or in frequency conversion. To this end, investigation of nonclassical properties of acoustic degrees of freedom is critical also for applications. Here, we investigate a strongly driven system consisting of a transmon qubit interacting with a high-overtone bulk acoustic resonator. We observe multiphonon transitions, which enable mapping the energy landscape in the coupled system. At a high driving amplitude comparable to the qubit-oscillator coupling, we observe a shift of the multiphonon spectral lines, reminiscent of Stark shift, which is explained using a simple model. Our work thus also provides insight in multiquanta transitions in other qubit-oscillator systems, not limited to acoustics or circuit quantum electrodynamics.

DOI: 10.1103/PhysRevApplied.17.064003

I. INTRODUCTION

Studies of micromechanical and acoustic modes have shed light on quantum properties of massive objects. Quantum properties have been experimentally verified in Gaussian oscillator states, showing, for example, entanglement between the vibrations of low-frequency drum oscillators [1–3]. States that are manifestly nonclassical, have also been created and measured. These include observations of the quantization of phonons [4–8], entanglement in the single-phonon limit [9], or entanglement mediated by acoustics [10]. Most of this work, based on electromechanics, relies on original work performed with superconducting qubits coupled to electromagnetic resonators [11], which revealed various electromagnetic quantum states following the verification of single-photon states in harmonic resonators [12–14], and later in magnon excitations [15]. Similar to purely electromagnetic quantum systems, micromechanical and acoustic resonators are emerging as promising components for quantum technology as they can exhibit low internal losses resulting in long excitation lifetimes, they are compact in size, and they can be coupled electromagnetically to a wide range of frequencies. Therefore, a detailed understanding of their quantum behavior is critical for future applications.

A nonlinear component, in electromechanics typically a superconducting qubit, is needed to prepare and detect energy quantization in an oscillator. Piezoelectric materials are found practical to obtain a sufficiently large resonant coupling between electromagnetics and acoustics. Several studies have shown the coupling of qubits to surface acoustic waves [16–18], where researchers were able to access the strong coupling regime and map out a prepared quantum state in the resonator [19]. Qubits have also been coupled to bulk acoustic waves [20]. A recently emerged system in this regard is a high-overtone bulk acoustic wave resonator (HBAR) [6,21–25], which is particularly exciting since it provides a large number of highly coherent acoustic modes [26] strongly coupled to the qubit.

In this work, we investigate a strongly driven quantum acoustic system. We address multiphonon transitions in a transmon qubit interacting with a HBAR resonator, which enable mapping the energy landscape in the coupled system. With superconducting qubits [27–29], and qubit-resonator systems [30–32], multiphoton transitions have been experimentally investigated in earlier work, however, they have received relatively little attention. In our work, we find an additional shift of the multiphonon spectral lines, reminiscent of Stark shift, which is explained using a simple model. Our work thus also provides insight in multiquanta transitions in generic qubit-oscillator systems.

II. THEORY

Let us study a basic system, where a qubit is transversely coupled to an oscillator, at the coupling energy g. The qubit has the ground and excited states $|g\rangle$ and $|e\rangle$, and the transition frequency ω_q. The oscillator's frequency

*mika.sillanpaa@aalto.fi

†A.V. and W.C. contributed equally to this work.

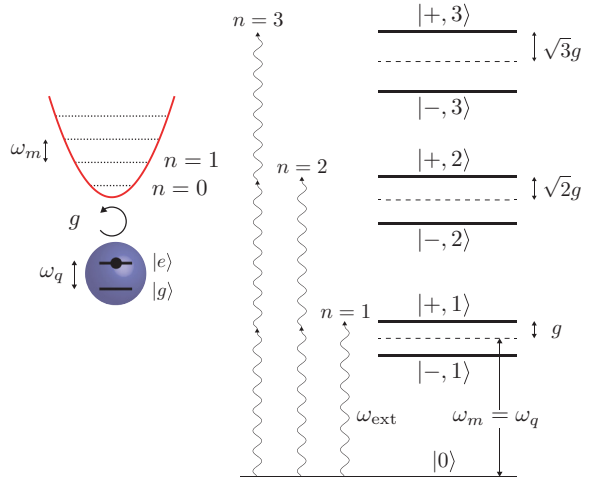

FIG. 1. *Multiquanta transitions in a qubit-oscillator system.* The transitions occur at the driving frequencies $\omega_{\rm ext} = \omega_{{\rm ext},n}$, in the pictured resonant case $\Delta = 0$ when $\omega_{\rm ext} = \omega_q \pm g/\sqrt{n}$.

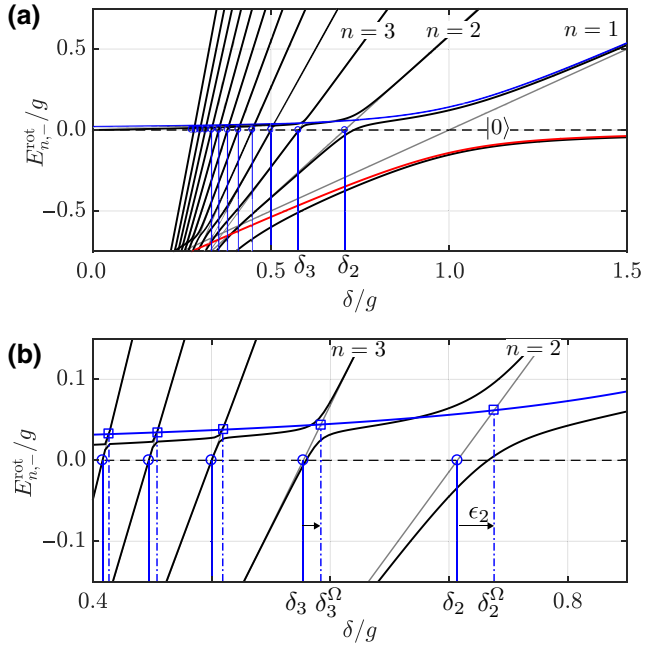

FIG. 2. *Multiquanta transitions in a rotating frame.* The qubit and the oscillator have detuning $\Delta = 0$. (a) The slanted gray lines are the energies of $|-,n\rangle$ when $\Omega = 0$, and the horizontal dashed line denotes the ground state $|g,0\rangle$. The black lines are for driving $\Omega/g = 0.4$, and are obtained from the full numerical solution of the driven system. The blue and red lines are from a TLS truncation of the full matrix. The blue vertical lines denote the multiphoton resonances δ_n, which are labeled for $n = 2, 3$. The first levels up to $n = 12$ are plotted. (b) Enlargement of (a). The dash-dotted vertical lines are the effective multiphoton resonances as shifted by the driving.

is ω_m, and the detuning from the qubit is defined as $\Delta = \omega_q - \omega_m$. The eigenstate energies become $E_{\pm,n} = n\omega_m \pm \frac{1}{2}\sqrt{4ng^2 + \Delta^2}$, for $n = 1, 2, \ldots$. The corresponding states $|\pm, n\rangle$ are hybridized from the qubit states and Fock states $|n\rangle$ of the oscillator. Additionally, the ground state $|0\rangle = |g, 0\rangle$ has the energy $E_0 = -\Delta/2$. In the resonant situation $\Delta = 0$, the energies $E_{\pm,n}$ exhibit a square-root dependence of the level repulsion on the oscillator quantum number n.

Now consider that the qubit is subject to a transverse drive with the Hamiltonian term $\Omega\cos(\omega_{\rm ext}t)\sigma_x$, where Ω is the Rabi frequency. With the system initialized in the ground state, multiquanta transitions can occur between the levels $|0\rangle$ and $|\pm, n\rangle$, when the frequency $\omega_{\rm ext}$ of the driving photons satisfies the condition $\omega_{{\rm ext},n} = E_{\pm,n} - E_0/n = \omega_m + \Delta/2n \pm \sqrt{\left(g/\sqrt{n}\right)^2 + (\Delta/2n)^2}$, which is pictured in Fig. 1. These are strongly suppressed processes of a higher order n, and thus, a relatively high driving is essential to observe them.

Similar to Ref. [33], we now move to a rotating frame defined by $\omega_{\rm ext}$. The detuning of the drive from the qubit is $\delta = \omega_q - \omega_{\rm ext}$. In this representation, the energies become $E^{\rm rot}_{n,\pm} = (\delta - \Delta)n \pm \frac{1}{2}\sqrt{4g^2n + \Delta^2}$. Without the driving, $\Omega = 0$, the energy levels $|\pm, n\rangle$ in this frame appear as the gray lines in Fig. 2(a), with a slope dependent on n. The frequencies at which each n level crosses the ground state $n = 0$ horizontal dashed line, correspond to the multiphoton spectral lines, with the detunings denoted as $\delta_n = \omega_q - \omega_{{\rm ext},n}$. These conditions are marked by circles in Fig. 2(a). However, as we see in the following, this picture is not yet complete, since it supposed $\Omega = 0$, and transitions cannot thus even occur.

In a qubit-oscillator system, multiquanta processes exhibit a feature that has been largely overlooked: the resonant conditions become power dependent unless $\Omega/g \ll 1$. In order to understand the case, we continue to work in the rotating frame, and introduce $\Omega \neq 0$. An anticrossing opens between the now-interacting levels $|0\rangle$ and $|\pm, 1\rangle$, with the gap given by $\Omega/\sqrt{2}$. Additionally, each $|\pm, n\rangle$, $n > 0$ level couples to all others. The dominant coupling is that between each level to $|\pm, 1\rangle$, which results in clear anticrossings as seen in Fig. 2.

The driven system is only analytically solvable for the fully resonant case ($\Delta = \delta = 0$) [34], however, we can make an approximation that each $n > 1$ state is predominantly independently hybridized with either $|-, 1\rangle$ or $|+, 1\rangle$, which implies restricting the full coupled system to a suitably chosen two-state truncation (Appendix A). Now, Fig. 2(b) allows for an intuitive explanation for how the multiquanta resonances shift from the intrinsic positions δ_n when the Rabi frequency Ω grows. As discussed above, the blue circles denote each $n > 1$ line crossing $n = 0$, which is the multiquanta resonance situation at a vanishing Ω. At higher Ω, the resonance condition, denoted by $\delta_n^\Omega \neq \delta_n$, shifts because of the crossing between higher-n levels and $|-, 1\rangle$ shifts. The shifted conditions are marked by squares

in Fig. 2(b). Notice the choice between $|-,1\rangle$ or $|+,1\rangle$ is based on the sign of Δ, and if $\Delta > \delta$ or the other way round.

The assumption that hybridization is strongly dominated by $|\pm,1\rangle$ also leads to an analytical solution for the shift. In the resonant case $\Delta = 0$, the result can be expressed in a simple form given in Appendix A, which can be further expanded up to a driving amplitude $\Omega/g \lesssim 1$ as

$$\epsilon_n \equiv \delta_n - \delta_n^{\Omega} \simeq \pm \frac{\Omega^2}{8g\left(n-\sqrt{n}\right)}, \quad n \geq 2, \qquad (1)$$

where the plus (minus) sign corresponds to the lower (upper) branch of the regular Jaynes-Cummings splitting. With the quadratic dependence of the shift on the Rabi frequency, the shift thus carries characteristics of the Stark shift.

In a general case $\Delta \neq 0$, the expressions for the shifted multiquanta conditions δ_n^{Ω} become more complicated (see Appendix A). Equation (1) for the shift itself, however, holds reasonably well also with a modest detuning $|\Delta| \lesssim g$.

III. EXPERIMENT

Our device layout is shown in Fig. 3(a). The qubit is of an "Xmon" [35] shape where one of the arms has a round pad to define an area of coupling with the HBAR chip. The HBAR resonator consists of a sapphire substrate of 250 μm thickness, on top of which there is a superconducting metallization layer made of molybdenum, which is finally covered by a piezo layer of 900-nm AlN. The sample design and fabrication are similar to those in Ref. [25]. The qubit-HBAR coupling energy is defined by the overlap of the qubit's electric field and of the strain profile of a given HBAR mode [22]. The intermediate metallization layer confines the electric field inside the piezo layer. This strongly enhances the qubit-HBAR coupling over that obtained without the metallization layer [6,22–24].

The HBAR chip is separate and mounted on top of the qubit circuit using a flip-chip technique. It is placed so that it only covers the round pad of the Xmon and no other circuit elements. The air gap between the piezo of the HBAR and the Xmon is estimated to be 1 μm. The qubit is excited through the measurement line.

The qubit state is measured dispersively using a readout resonator with frequency $\omega_r/2\pi = 6.014$ GHz. The qubit frequency is tunable via the flux bias and has a maximum frequency of $\omega_q/2\pi = 4.661$ GHz with a T_1 limited linewidth of $\gamma/2\pi \simeq 0.2$ MHz. We apply a coherent drive that drives the qubit transversely as discussed above. This excitation rf signal is applied to the qubit via the readout resonator. The Rabi frequency is calibrated by fitting power-dependent spectra using a model of a qubit coupled to a harmonic mode. A discussion of the calibration can be found in Appendix B.

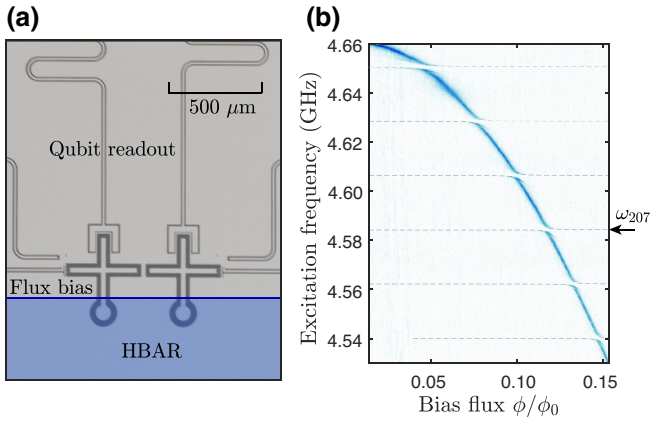

FIG. 3. *Schematics of the experiment.* (a) Sample layout. The device includes two coupled qubits, each separately coupled to a HBAR resonator defined by either qubit's electrode. In the experiment, only one of the qubit-HBAR systems is studied, which is achieved by detuning the other qubit. Location of the HBAR flip chip is sketched on top of the micrograph. (b) Two-tone spectroscopy of the qubit. The avoided crossing with several HBAR modes, whose frequencies are shown by dashed lines, are visible. Mode number 207 is shown for reference.

Figure 3(b) shows a sweep of the qubit frequency through HBAR modes between 4.54 and 4.66 GHz. A fit using a multimodal model gives a free spectral range (FSR) of 22.15 MHz, which agrees with the sapphire thickness of 250 μm and sound velocity 11100 m/s. The coupling between the qubit and a single mode is $g/2\pi = 1.45 \pm 0.2$ MHz, also being subject to little variation with frequency.

We now increase the excitation amplitude Ω to disclose the multiphonon transitions between the ground state and $|\pm,n\rangle$. The transitions involve hybridized levels of the qubit and acoustics, and thus we use the label multiphonon to highlight the role of phonons. Figures 4(a) and 4(b) demonstrate the appearance of multiphonon transition lines at two drive powers $\Omega \simeq 0.7g$ and $2.1g$. The multimodal model is plotted on top of the 2D data (solid black) and its fit gives the mode frequencies and coupling. These values are used to calculate the power-dependent shifts in the second (dashed dark blue) and the third (dashed light blue) manifolds with no fitting using our model described above. In Fig. 4(b), the faint diagonal features in the top right and bottom left are the $0 \rightarrow 2\pm$ transitions of neighboring acoustic overtone modes.

Figure 4(c) displays individual resonance curves from line cuts of (a) and (b) as well as from a third sweep at higher driving power. The dashed horizontal lines indicate the intrinsic multiphonon resonant frequencies $n = 2, 3, 4$, with the expected driving-induced shifts indicated by the colored arrows. The black arrows indicate the dressed

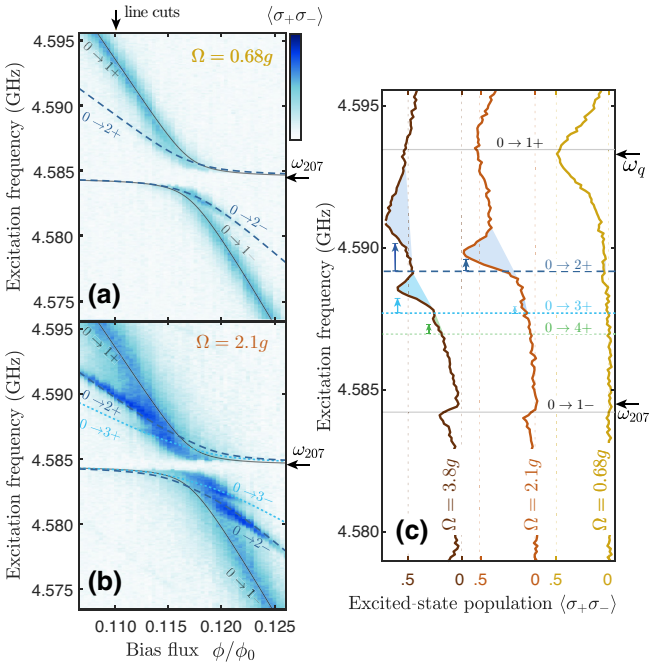

FIG. 4. *Multiphonon transitions.* (a) Two-tone spectroscopy at a modest Rabi frequency $\Omega \simeq 0.68g$. The first $n = 2$ multiphonon resonance line (blue) is visible. (b) Higher driving $\Omega \simeq 2.1g$. The lines $n = 2, 3$ are visible. (c) Line cuts from the two-dimensional (2D) data at the detuning $\Delta/2\pi \simeq 8.8$ MHz, indicated by the arrow at the top, for three drive powers $\Omega \simeq 0.7g, 2.1g, 3.8g$. The intrinsic multiphonon resonance conditions for $n = 2, 3, 4$ (blue, cyan, green) are marked with dashed horizontal lines. The expected driving-induced shifts are indicated by the arrows. The black lines show the frequencies of the dressed states of a multimode system with the labeled black arrows denoting the bare qubit ω_q and mode frequency ω_{207} values.

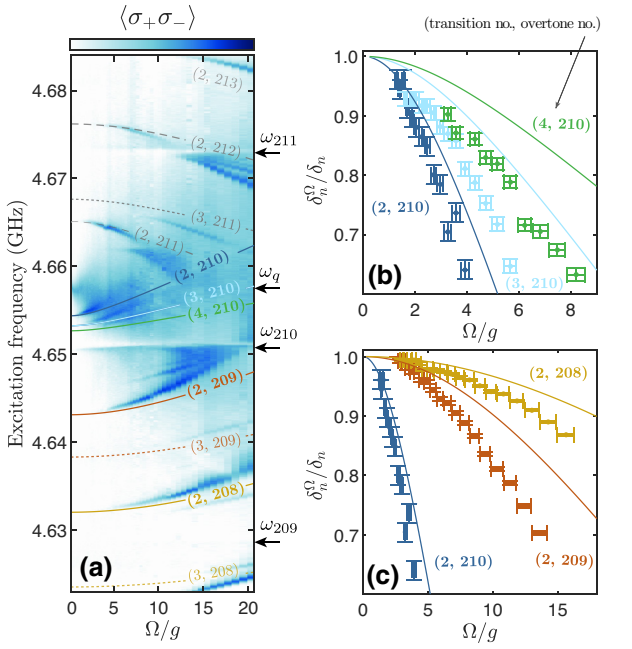

FIG. 5. *Dressing of the multiphonon transitions.* (a) The power dependence of the multiphonon transitions when the qubit is detuned a distance $\Delta \simeq 3.9g$ from the mode ω_{210} at 4.651 GHz. The dashed lines are the analytical result based on TLS approximation of the driving-induced hybridization (see Appendix A) and are labeled (n, m) according to the multiphonon number n and mechanical mode number m. Panels (b) and (c) focus on the transitions marked by solid lines. (b) The extracted frequencies of the multiphonon peaks for mode $m = 210$ and multiphonon numbers $n = 2, 3, 4$ (blue, cyan, and green points) are shown versus the calibrated Rabi frequency normalized by coupling. The analytical result is represented by the solid lines. (c) Frequencies of the multiphonon peak $n = 2$ for modes $m = 208, 209, 210$ are shown with the analytical result in a similar manner to (b). The qubit frequency is $\omega_q/2\pi = 4.657$ GHz.

qubit and harmonic mode frequencies, which at a detuning of $\Delta = 6g$ are close to their bare values.

Finally, we investigate in detail the shifts of the multiphonon resonance conditions. In Fig. 5 we display the power dependence of the spectrum, demonstrating agreement with the model at low powers. In (a), the data illustrates the multitude of transitions, as well as the power-dependent shifts, due to several HBAR modes and their individual manifolds n.

Using our simple model restricting to a single harmonic mode, we can cover most of the apparent multiphonon transitions including the power dependence, while not being limited to the nearest-mode interactions. In Fig. 5(a), other transitions that have not been labeled can also be seen. We find that these are explained by multimode multiphonon interactions, which we leave outside the scope of this paper.

The (b) and (c) in Fig. 5 analyze in detail the validity of our simple model (dashed line) in explaining the multiphonon transition frequency data and their power-dependent shifts in the near resonant and detuned cases. Panel (b) shows the second (blue), third (cyan), and fourth (green) excitation manifolds, when treating the nearest acoustic mode below, while (c) shows the second excitation manifold when treating the three modes below the qubit. The vertical axis have been scaled by δ_n which are the intrinsic resonance conditions. The data points in (b) and (c) are extracted by locating the peak positions from (a).

Instead of the $\sqrt{n}$ scaling in the upper manifolds, in our off-resonant situation the scaling is modified to $\sqrt{n + (\Delta'/2)^2}$ where Δ' gives the detuning in units of g ($\Delta = \Delta' g$). This is illustrated in Fig. 5(b) where the peak position data has been scaled by δ_n. The intrinsic resonance conditions are given by $\delta_n^\Omega/\delta_n = 1$, and it can be seen that the data converges towards this point.

IV. DISCUSSION

We now discuss the limitations of the simple two-level system (TLS) model. We assume in the model derivation

that the different multiquanta transitions are independent. However, the different transitions exhibit coupling with each other. The consequences of the coupling can be pictured based on Fig. 2, where the anticrossings are seen to exhibit overlap, which becomes more pronounced with increased Ω. The couplings induce level repulsion, thus pushing the multiquanta anticrossings towards the qubit and oscillator branches.

One can see from this picture that the initial spacing of the anticrossings (based on the detuning Δ) affects the range of driving powers where the model makes a good prediction. The anticrossing size depends strongly on the drive power and the detuning only affects this weakly. So in the case of large detuning, the qubitlike states are initially spread out in frequency and so the anticrossing overlap becomes more relevant at a higher power as compared to the resonant case. The oscillatorlike states for large detuning are however bunched together and therefore the model does not predict their behavior as well in this case, and so these branches are not plotted on Fig. 5. This means that the TLS model better predicts the multiquanta transitions in the detuned case. This is clearly seen in Figs. 5(b) and 5(c), where the more detuned case (c) shows a better match to the TLS model.

The resolution of individual multiphonon transitions is dependent on the quality factor of the acoustic mode as well as the decay and dephasing times of the transmon and the detuning Δ. At our parameters, we can optimally observe the transitions up to $n = 4$. On resonance, $\Delta = 0$, the multiphonon transitions cannot be distinguished due to the acoustic mode quality factor and so for a more detailed observation of the power dependence, we have to look at the off-resonant case.

Since the anharmonicity of the transmon qubit is relatively small as compared to the level spacing, it is worth looking at the influence of the higher transmon levels on the two-quanta transitions. We diagonalize a more accurate system consisting of many transmon levels, and find that two-phonon transitions at zero power would be shifted down in frequency compared to the TLS model by around 10 kHz when $\Delta > 0$, and shifted up in frequency by around 20 kHz when $\Delta < 0$. These shifts are negligible within the experimental resolution, and thus the TLS approximation is expected to give a proper description of the system.

The understanding of multiquanta transition frequencies in qubit-oscillator systems in general can be of use in recognizing possible outcomes in quantum technology, e.g., in avoiding accidental resonant excitations, or in designing a measurement scheme that utilizes specific (multimode) transitions. Our model provides a computationally effective means of estimating the transition frequencies with a possibility to account for multiple modes.

To conclude, we investigate multiphonon transitions in an acoustic resonator coupled to a superconducting qubit. Besides providing further, strong evidence of energy quantization of phonons, we address a power-induced shift of the multiphonon resonances, associated to hybridization of the individual multiquanta processes.

ACKNOWLEDGMENTS

We acknowledge the facilities and technical support of Otaniemi research infrastructure for Micro and Nanotechnologies (OtaNano) that is part of the European Microkelvin Platform. This work is supported by the Academy of Finland (Contracts No. 307757 and No. 312057), by the European Research Council (615755-CAVITYQPD), by the Wihuri Foundation, and by the Aalto Centre for Quantum Engineering. The work is performed as part of the Academy of Finland Centre of Excellence program (Project No. 336810). We acknowledge funding from the European Union's Horizon 2020 research and innovation program under Grant Agreement No. 732894 (FETPRO HOT).

APPENDIX A: STARK SHIFT OF THE MULTIPHOTON SPECTRAL LINES

The qubit-oscillator system, where the qubit is driven by a strong transverse field, is described by

$$H = -\frac{\omega_q}{2}\sigma_z + \omega_m(a^\dagger a + 1/2) + g(a^\dagger + a)\sigma_x + \Omega\cos(\omega_{\rm ext}t)\sigma_x. \tag{A1}$$

Here, Ω is the Rabi frequency, and $\omega_{\rm ext} \approx \omega_q$ is the frequency of the drive.

In the rotating frame defined by $\omega_{\rm ext}$, Eq. (A1) becomes

$$H = (\delta - \Delta)\left(a^\dagger a + \frac{1}{2}\right) - \frac{\delta}{2}\sigma_z + g(a^\dagger\sigma^- + a\sigma^+) + \frac{\Omega}{2}\sigma_x. \tag{A2}$$

Here, the qubit-drive detuning is $\delta = \omega_q - \omega_{\rm ext}$, and qubit-oscillator detuning $\Delta = \omega_q - \omega_m$.

Without driving, i.e., $\Omega = 0$, the energies in this frame are those of the Jaynes-Cummings system:

$$E_{\pm,n} = n(\delta - \Delta) \pm \frac{1}{2}\sqrt{4ng^2 + \Delta^2}\,, \quad n \geq 1, \tag{A3}$$

and the ground-state energy is $E_0 = -\frac{1}{2}\Delta$. The corresponding states, again without driving, are

$$\begin{aligned} |0\rangle &= |g, 0\rangle, \\ |+, n\rangle &= C|e, n\rangle + S|g, n+1\rangle, \\ |-, n\rangle &= -S|e, n\rangle + C|g, n+1\rangle. \end{aligned} \tag{A4}$$

In Eq. (A4) and below, we are using a shorthand notation $S = \sin\Theta_n$, $C = \cos\Theta_n$, and $\tan 2\Theta_n = 2g\sqrt{n+1}/\Delta$.

The multiquanta transitions based on Eq. (A3) occur if the ground-state energy equals those of higher n, i.e., $E_{\pm,n} = E_0$. This occurs at the drive detuning

$$\delta_n = \frac{\mp\frac{1}{2}\sqrt{4g^2n + \Delta^2} - \frac{1}{2}\Delta}{n} + \Delta, \tag{A5}$$

or equivalently, when the driving frequency satisfies the condition

$$\omega_{\text{ext}} = \frac{\pm\frac{1}{2}\sqrt{4g^2n + \Delta^2} + \frac{1}{2}\Delta}{n} + \omega_m. \tag{A6}$$

At $\Delta = 0$, Eq. (A5) reduces to

$$\delta_n = \mp\frac{g}{\sqrt{n}}. \tag{A7}$$

We now include the driving, $\Omega \neq 0$. Equation (A2) in this case is not analytically solvable any more. We can, however, find approximate results. We work in the bare state basis,

$$\Psi = \sum_{k,l} c_{gk}|g,k\rangle + c_{el}|e,l\rangle. \tag{A8}$$

Inserting Eq. (A8) into Eq. (A2) results in an infinite matrix, in which we now restrict to the three lowest basis states:

$$\begin{bmatrix} -\frac{1}{2}\Delta & 0 & \frac{1}{2}\Omega \\ 0 & \delta - \frac{3}{2}\Delta & g \\ \frac{1}{2}\Omega & g & \delta - \frac{1}{2}\Delta \end{bmatrix} \begin{bmatrix} c_{g0} \\ c_{g1} \\ c_{e0} \end{bmatrix} = E \begin{bmatrix} c_{g0} \\ c_{g1} \\ c_{e0} \end{bmatrix}. \tag{A9}$$

The driving creates excitations from the ground state to $|e1\rangle$, or, equivalently, to the second Jaynes-Cummings doublet. This renders the system nonblockdiagonal.

Next, we rotate Eq. (A9) to the eigenbasis:

$$H' = UHU^{-1} \tag{A10}$$

with

$$U = \begin{bmatrix} 1 & 0 & 0 \\ 0 & S & C \\ 0 & C & -S \end{bmatrix}. \tag{A11}$$

The result is

$$H' = \begin{bmatrix} -\frac{\Delta}{2} & \frac{1}{2}C\Omega & -\frac{1}{2}S\Omega \\ \frac{1}{2}C\Omega & C^2\left(\delta - \frac{\Delta}{2}\right) + 2CSg + S^2\left(\delta - \frac{3\Delta}{2}\right) & C^2g - CS\Delta - gS^2 \\ -\frac{1}{2}S\Omega & C^2g - CS\Delta - gS^2 & C^2\left(\delta - \frac{3\Delta}{2}\right) - 2CgS + \frac{1}{2}S^2(2\delta - \Delta) \end{bmatrix}, \tag{A12}$$

expressed in the basis $[|0\rangle, |-,1\rangle, |+,1\rangle]^T$. From Eq. (A12), we can now make an approximation that we select a 2×2 subspace that couples the ground state to either $|-,1\rangle$ or $|+,1\rangle$.

The subspace is determined by if $\delta \geq \Delta$, or the other way round. First we discuss the situation $\delta \geq \Delta$, where the relevant block is that coupling $|0\rangle \Longleftrightarrow |-,1\rangle$:

$$H_2 = \begin{bmatrix} -\frac{\Delta}{2} & -\frac{1}{2}S\Omega \\ -\frac{1}{2}S\Omega & C^2\left(\delta - \frac{3\Delta}{2}\right) - 2CSg + \frac{1}{2}S^2(2\delta - \Delta) \end{bmatrix}. \tag{A13}$$

We now treat the resonant condition $\Delta = 0$. Equation (A13) diagonalizes with the energies

$$E_{2,\pm} = \pm\frac{1}{4}\sqrt{(2\delta - 2g)^2 + 2\Omega^2} + \frac{1}{2}(\delta - g). \tag{A14}$$

Equation (A14) illustrates how the lowest Jaynes-Cummings doublet is split by the driving. Further, when $\delta = g$ a gap equal to $\Omega/\sqrt{2}$ opens, which means the system undergoes oscillations between the ground state and the first Jaynes-Cummings doublet.

Although Eq. (A2) describes a coupled infinite-level system, we can approximate that the dominant coupling due to the driving is the hybridization of the levels of $n > 2$ with the energy levels in Eq. (A14). This is illustrated in Fig. 2 in the main text, which also shows how the shift of the multiphoton transitions can be simply pictured as arising from dressing with Eq. (A14). The levels E_2 cross the undriven energies $E_{\pm,n}$ as given by Eq. (A3), at a driving frequency that satisfies

$$E_{-,n} = E_{2,+}, \quad n \geq 2, \tag{A15}$$

which provides n dependence for the shift.

1. Resonant case $\Delta = 0$

If $\Delta = 0$, Eq. (A15) reads

$$\delta n - g\sqrt{n} = \frac{1}{4}\sqrt{4(\delta + g)^2 + 2\Omega^2} + \frac{1}{2}(\delta + g), \tag{A16}$$

and yields the positions of the multiphoton resonances:

$$\delta_n^{\Omega} = \frac{\sqrt{4g^2 n\left(\sqrt{n}-1\right)^2 + 2(n-1)n\Omega^2} + 2g\sqrt{n}\left(2n-\sqrt{n}-1\right)}{4(n-1)n}. \tag{A17}$$

The corresponding shift of the multiphonon resonance due to the driving, up to fourth order in Ω, becomes

$$\epsilon^{\Omega} \equiv \delta_n - \delta_n^{\Omega} \simeq \frac{\Omega^2}{8g\left(n-\sqrt{n}\right)} - \frac{\left(\sqrt{n}+1\right)\Omega^4}{64g^3\left(\sqrt{n}-1\right)^2\sqrt{n}}, \quad n \geq 2. \tag{A18}$$

If $\delta < \Delta$, we consider the block that couples $|0\rangle \Longleftrightarrow |+,1\rangle$. We obtain, similar to Eq. (A13):

$$H_2 = \begin{bmatrix} -\frac{\Delta}{2} & \frac{C\Omega}{2} \\ \frac{C\Omega}{2} & C^2\left(\delta-\frac{\Delta}{2}\right) + 2CgS + S^2\left(\delta-\frac{3\Delta}{2}\right) \end{bmatrix}. \tag{A19}$$

In the resonant situation $\Delta = 0$, we obtain from Eq. (A19) the energies

$$E_{2,\pm} = \pm\frac{1}{4}\sqrt{(2\delta+2g)^2+2\Omega^2} + \frac{1}{2}(\delta+g), \tag{A20}$$

and the multiphoton resonances become, by symmetry, those in Eq. (A17) but with a minus sign in front.

2. Analytical solutions, $\Delta \neq 0$

Next we collect analytical solutions for arbitrary Δ in four different situations depending on the signs of δ and Δ. There are two sets of energy levels from the TLS approximation, Eqs. (A13) and (A19), given as

$$E_{2,\pm}^{-} = \frac{1}{4}\left(2\delta - \Delta\cos 2\Theta - 3\Delta - 2g\sin 2\Theta \pm \sqrt{(-2\delta+\Delta\cos 2\Theta+\Delta+2g\sin 2\Theta)^2 + 4\Omega^2\sin^2\Theta}\right), \tag{A21}$$

$$E_{2,\pm}^{+} = \frac{1}{4}\left(2\delta + \Delta\cos 2\Theta - 3\Delta + 2g\sin 2\Theta \pm \sqrt{(2\delta+\Delta\cos 2\Theta-\Delta+2g\sin 2\Theta)^2 + 4\Omega^2\cos^2\Theta}\right). \tag{A22}$$

Let us use a shorthand notation:

$$\begin{aligned} \Delta_{gn} &= \sqrt{4g^2 n + \Delta^2}, \\ \Delta_{g1} &= \sqrt{4g^2 + \Delta^2}. \end{aligned} \tag{A23}$$

a. $\Delta \geq 0, \delta \geq \Delta$

TLS energies are given by $E_{2,+}^{-}$ in Eq. (A21), and the positions of the multiquanta resonances satisfy

$$\begin{aligned} 4(n-1)n\delta_n^{\Omega} = &\sqrt{2\Delta^2\left(1-(n-1)n\left(\frac{\Delta_{g1}}{\Delta}-1\right)\right) + 2\left(-n\frac{\Delta_{g1}}{\Delta}+n-1\right)\Delta\Delta_{gn} + 4(n-1)n\Omega^2\sin^2\frac{\Theta}{2} + 4g^2 n(n+1)} \\ &- \Delta n\left(\frac{\Delta_{g1}}{\Delta}+5\right) + \Delta_{gn}(2n-1) + \Delta(4n^2+1). \end{aligned} \tag{A24}$$

b. $\Delta \geq 0, \delta < \Delta$

TLS energies are given by $E_{2,-}^{+}$ Eq. (A22), while the positions of the multiquanta resonances satisfy

$$\begin{aligned} 4(n-1)n\delta_n^{\Omega} = &-\sqrt{2\Delta^2\left((n-1)n\left(\frac{\Delta_{g1}}{\Delta}+1\right)+1\right) - 2\left(n\frac{\Delta_{g1}}{\Delta}+n-1\right)\Delta\Delta_{gn} + 4(n-1)n\Omega^2\cos^2\frac{\Theta}{2} + 4g^2 n(n+1)} \\ &+ \Delta n\left(\frac{\Delta_{g1}}{\Delta}+4n-5\right) + \Delta_{gn}(1-2n) + \Delta. \end{aligned} \tag{A25}$$

c. $\Delta < 0, \delta > \Delta$

TLS energies are given by $E^{+}_{2,+}$ Eq. (A22), while the positions of the multiquanta resonances satisfy

$$4(n-1)n\delta_n^{\Omega} = \sqrt{2\Delta^2\left((n-1)n\left(\frac{\Delta_{g1}}{\Delta}+1\right)+1\right)+2\left(n\frac{\Delta_{g1}}{\Delta}+n-1\right)\Delta\Delta_{gn}+4(n-1)n\Omega^2\cos^2\frac{\Theta}{2}+4g^2n(n+1)}$$
$$+\Delta n\left(\frac{\Delta_{g1}}{\Delta}+4n-5\right)+\Delta_{gn}(2n-1)+\Delta. \tag{A26}$$

d. $\Delta < 0, \delta < \Delta$

TLS energies given by $E^{-}_{2,-}$ Eq. (A21), while the positions of the multiquanta resonances satisfy

$$4(n-1)n\delta_n^{\Omega} = -\sqrt{2\Delta^2\left(1-(n-1)n\left(\frac{\Delta_{g1}}{\Delta}-1\right)\right)+2\left(n\frac{\Delta_{g1}}{\Delta}-n+1\right)\Delta\Delta_{gn}+4(n-1)n\Omega^2\sin^2\frac{\Theta}{2}+4g^2n(n+1)}$$
$$-\Delta n\left(\frac{\Delta_{g1}}{\Delta}+5\right)+\Delta_{gn}(1-2n)+\Delta(4n^2+1). \tag{A27}$$

APPENDIX B: RABI POWER CALIBRATION

The calibration of the qubit drive can usually be performed by considering the broadening of its linewidth with power according to $\delta\omega = 2\sqrt{\gamma_{\rm tot}/\gamma\,\Omega^2+\gamma_{\rm tot}^2}$ where $\gamma_{\rm tot} = \gamma/2+\gamma_\phi$ and γ and γ_ϕ are related to the usual qubit decay and dephasing. There is a linear correspondence between the applied driving P and Rabi frequency: $P = \eta\Omega$ where the calibration parameter η is found by fitting the total linewidth to the applied driving. In this scheme, a reliable determination of η requires consideration of the higher driving, where $\Omega \gg \gamma_{\rm tot}$.

In our case, we cannot well reach this limit, since we are limited to low powers where $\Omega \ll$ FSR. Otherwise, coupling to the acoustic modes has a complicated effect on the qubit spectrum. The Rabi frequency is therefore calibrated by fitting the spectra using Qutip simulations with a system of a qubit coupled to two modes for a dedicated set of calibration data, where the qubit lies between two modes.

Pictured in Fig. 6(b) is a Qutip simulation showing the multiquanta resonances for a qubit coupled to one mode. This can be compared with the measurement data in (a), which is the same as Fig. 5 to confirm the Rabi frequency calibration. In the figure, the solid lines are those predicted by the TLS model. Additionally, we show the results of including a phenomenological scaling factor for the driving in order to improve the TLS model. This is showed by the dashed lines, which closely follow the data. Panels (c) and (d) show the improvement in more detail. We find that a scaling factor (approximately $1.4\times\Omega$) improves the accuracy of the model, which underestimates the shift. The rationale for a possible scaling factor, which is larger than one, is that the TLS model does not take into account

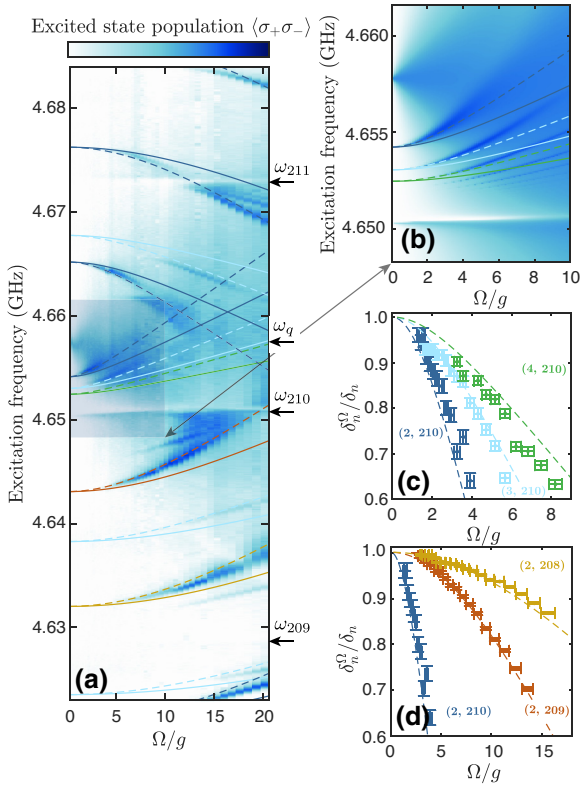

FIG. 6. *Rabi frequency calibration*. (a) The data in Fig. 5 replotted. Solid lines represent the TLS model based on calibration, while the dashed lines include a scaling factor to account for coupling between different multiphoton transitions. (b) Corresponding numerical simulation of the qubit population with one harmonic mode, showing the shaded rectangle in (a). The data points from Figs. 5(b) and 5(c) are plotted in (c),(d), respectively, against the TLS model using the scaling factor (dashed).

the drive-induced coupling of the higher excitation manifolds, which repel the multiquanta anticrossings towards the qubit and oscillator branches. At small Δ, the individual anticrossings overlap, and thus the TLS model is expected to be more valid at large Δ.

[1] C. F. Ockeloen-Korppi, E. Damskägg, J. M. Pirkkalainen, M. Asjad, A. A. Clerk, F. Massel, M. J. Woolley, and M. A. Sillanpää, Stabilized entanglement of massive mechanical oscillators, Nature **556**, 478 (2018).

[2] Shlomi Kotler, Gabriel A. Peterson, Ezad Shojaee, Florent Lecocq, Katarina Cicak, Alex Kwiatkowski, Shawn Geller, Scott Glancy, Emanuel Knill, Raymond W. Simmonds, José Aumentado, and John D. Teufel, Direct observation of deterministic macroscopic entanglement, Science **372**, 622 (2021).

[3] Laure Mercier de Lépinay, Caspar F. Ockeloen-Korppi, Matthew J. Woolley, and Mika A. Sillanpää, Quantum mechanics-free subsystem with mechanical oscillators, Science **372**, 625 (2021).

[4] Justin D. Cohen, Seán M. Meenehan, Gregory S. MacCabe, Simon Gröblacher, Amir H. Safavi-Naeini, Francesco Marsili, Matthew D. Shaw, and Oskar Painter, Phonon counting and intensity interferometry of a nanomechanical resonator, Nature **520**, 522 (2015).

[5] Sungkun Hong, Ralf Riedinger, Igor Marinković, Andreas Wallucks, Sebastian G. Hofer, Richard A. Norte, Markus Aspelmeyer, and Simon Gröblacher, Hanbury Brown and Twiss interferometry of single phonons from an optomechanical resonator, Science **358**, 203 (2017).

[6] Yiwen Chu, Prashanta Kharel, Taekwan Yoon, Luigi Frunzio, Peter T. Rakich, and Robert J. Schoelkopf, Creation and control of multi-phonon Fock states in a bulk acoustic-wave resonator, Nature **563**, 666 (2018).

[7] L. R. Sletten, B. A. Moores, J. J. Viennot, and K. W. Lehnert, Resolving Phonon Fock States in a Multimode Cavity with a Double-Slit Qubit, Phys. Rev. X **9**, 021056 (2019).

[8] Patricio Arrangoiz-Arriola, E. Alex Wollack, Zhaoyou Wang, Marek Pechal, Wentao Jiang, Timothy P. McKenna, Jeremy D. Witmer, Raphaël Van Laer, and Amir H. Safavi-Naeini, Resolving the energy levels of a nanomechanical oscillator, Nature **571**, 537 (2019).

[9] Ralf Riedinger, Andreas Wallucks, Igor Marinković, Clemens Löschnauer, Markus Aspelmeyer, Sungkun Hong, and Simon Gröblacher, Remote quantum entanglement between two micromechanical oscillators, Nature **556**, 473 (2018).

[10] A. Bienfait, K. J. Satzinger, Y. P. Zhong, H.-S. Chang, M.-H. Chou, C. R. Conner, É. Dumur, J. Grebel, G. A. Peairs, R. G. Povey, and A. N. Cleland, Phonon-mediated quantum state transfer and remote qubit entanglement, Science **364**, 368 (2019).

[11] A. Wallraff, D. I. Schuster, L. Frunzio A. Blais, R.-S. Huang, J. Majer, S. Kumar, S. M. Girvin, and R. J. Schoelkopf, Strong coupling of a single photon to a superconducting qubit using circuit quantum electrodynamics, Nature **431**, 162 (2004).

[12] D. I. Schuster, A. A. Houck, J. A. Schreier, A. Wallraff, J. M. Gambetta, A. Blais, L. Frunzio, J. Majer, B. Johnson, M. H. Devoret, S. M. Girvin, and R. J. Schoelkopf, Resolving photon number states in a superconducting circuit, Nature **445**, 515 (2007).

[13] J. M. Fink, M. Göppl, M. Baur, R. Bianchetti, P. J. Leek, A. Blais, and A. Wallraff, Climbing the Jaynes–Cummings ladder and observing its $\sqrt{n}$ nonlinearity in a cavity QED system, Nature **454**, 315 (2008).

[14] Mario F. Gely, Marios Kounalakis, Christian Dickel, Jacob Dalle, Rémy Vatré, Brian Baker, Mark D. Jenkins, and Gary A. Steele, Observation and stabilization of photonic Fock states in a hot radio-frequency resonator, Science **363**, 1072 (2019).

[15] Dany Lachance-Quirion, Yutaka Tabuchi, Seiichiro Ishino, Atsushi Noguchi, Toyofumi Ishikawa, Rekishu Yamazaki, and Yasunobu Nakamura, Resolving quanta of collective spin excitations in a millimeter-sized ferromagnet, Sci. Adv. **3**, e1603150 (2017).

[16] Martin V. Gustafsson, Thomas Aref, Anton Frisk Kockum, Maria K. Ekström, Göran Johansson, and Per Delsing, Propagating phonons coupled to an artificial atom, Science **346**, 207 (2014).

[17] Riccardo Manenti, Anton F. Kockum, Andrew Patterson, Tanja Behrle, Joseph Rahamim, Giovanna Tancredi, Franco Nori, and Peter J. Leek, Circuit quantum acoustodynamics with surface acoustic waves, Nat. Commun. **8**, 1 (2017).

[18] Bradley A. Moores, Lucas R. Sletten, Jeremie J. Viennot, and K. W. Lehnert, Cavity Quantum Acoustic Device in the Multimode Strong Coupling Regime, Phys. Rev. Lett. **120**, 227701 (2018).

[19] K. J. Satzinger, Y. P. Zhong, H. S. Chang, G. A. Peairs, A. Bienfait, Ming-Han Chou, A. Y. Cleland, C. R. Conner, É. Dumur, J. Grebel, I. Gutierrez, B. H. November, R. G. Povey, S. J. Whiteley, D. D. Awschalom, D. I. Schuster, and A. N. Cleland, Quantum control of surface acoustic-wave phonons, Nature **563**, 661 (2018).

[20] A. D. O'Connell, M. Hofheinz, M. Ansmann, Radoslaw C. Bialczak, M. Lenander, Erik Lucero, M. Neeley, D. Sank, H. Wang, M. Weides, J. Wenner, John M. Martinis, and A. N. Cleland, Quantum ground state and single-phonon control of a mechanical resonator, Nature **464**, 697 (2010).

[21] Xu Han, Chang-Ling Zou, and Hong X. Tang, Multimode Strong Coupling in Superconducting Cavity Piezoelectromechanics, Phys. Rev. Lett. **117**, 123603 (2016).

[22] Yiwen Chu, Prashanta Kharel, William H. Renninger, Luke D. Burkhart, Luigi Frunzio, Peter T. Rakich, and Robert J. Schoelkopf, Quantum acoustics with superconducting qubits, Science **358**, 199 (2017).

[23] Mikael Kervinen, Ilkka Rissanen, and Mika Sillanpää, Interfacing planar superconducting qubits with high overtone bulk acoustic phonons, Phys. Rev. B **97**, 205443 (2018).

[24] Mikael Kervinen, Jhon E. Ramírez-Muñoz, Alpo Välimaa, and Mika A. Sillanpää, Landau-Zener-Stückelberg Interference in a Multimode Electromechanical System in the Quantum Regime, Phys. Rev. Lett. **123**, 240401 (2019).

[25] Mikael Kervinen, Alpo Välimaa, Jhon E. Ramírez-Muñoz, and Mika A. Sillanpää, Sideband Control of a Multimode

Quantum Bulk Acoustic System, Phys. Rev. Appl. **14**, 054023 (2020).

[26] Vikrant J. Gokhale, Brian P. Downey, D. Scott Katzer, Neeraj Nepal, Andrew C. Lang, Rhonda M. Stroud, and David J. Meyer, Epitaxial bulk acoustic wave resonators as highly coherent multi-phonon sources for quantum acoustodynamics, Nat. Commun. **11**, 2314 (2020).

[27] Y. Nakamura, Yu. A. Pashkin, and J. S. Tsai, Rabi Oscillations in a Josephson-Junction Charge Two-Level System, Phys. Rev. Lett. **87**, 246601 (2001).

[28] S. Saito, M. Thorwart, H. Tanaka, M. Ueda, H. Nakano, K. Semba, and H. Takayanagi, Multiphoton Transitions in a Macroscopic Quantum Two-State System, Phys. Rev. Lett. **93**, 037001 (2004).

[29] V. I. Shnyrkov, Th. Wagner, D. Born, S. N. Shevchenko, W. Krech, A. N. Omelyanchouk, E. Il'ichev, and H. G. Meyer, Multiphoton transitions between energy levels in a phase-biased Cooper-pair box, Phys. Rev. B **73**, 024506 (2006).

[30] A. Wallraff, D. I. Schuster, A. Blais, J. M. Gambetta, J. Schreier, L. Frunzio, M. H. Devoret, S. M. Girvin, and R. J. Schoelkopf, Sideband Transitions and Two-Tone Spectroscopy of a Superconducting Qubit Strongly Coupled to an On-Chip Cavity, Phys. Rev. Lett. **99**, 050501 (2007).

[31] Frank Deppe, Matteo Mariantoni, E. P. Menzel, A. Marx, S. Saito, K. Kakuyanagi, H. Tanaka, T. Meno, K. Semba, H. Takayanagi, E. Solano, and R. Gross, Two-photon probe of the Jaynes–Cummings model and controlled symmetry breaking in circuit QED, Nat. Phys. **4**, 686 (2008).

[32] Lev S. Bishop, J. M. Chow, Jens Koch, A. A. Houck, M. H. Devoret, E. Thuneberg, S. M. Girvin, and R. J. Schoelkopf, Nonlinear response of the vacuum Rabi resonance, Nat. Phys. **5**, 105 (2009).

[33] V. Peano and M. Thorwart, Quasienergy description of the driven Jaynes-Cummings model, Phys. Rev. B **82**, 155129 (2010).

[34] P. Alsing, D.-S. Guo, and H. J. Carmichael, Dynamic Stark effect for the Jaynes-Cummings system, Phys. Rev. A **45**, 5135 (1992).

[35] R. Barends, J. Kelly, A. Megrant, D. Sank, E. Jeffrey, Y. Chen, Y. Yin, B. Chiaro, J. Mutus, C. Neill, P. O'Malley, P. Roushan, J. Wenner, T. C. White, A. N. Cleland, and John M. Martinis, Coherent Josephson Qubit Suitable for Scalable Quantum Integrated Circuits, Phys. Rev. Lett. **111**, 080502 (2013).